

NOTE

Detection of nanotesla AC magnetic fields using steady-state SIRS and ultra-low field MRI

To cite this article: Bragi Sveinsson *et al* 2020 *J. Neural Eng.* 17 034001

View the [article online](#) for updates and enhancements.



The Department of Bioengineering at the University of Pittsburgh Swanson School of Engineering invites applications from accomplished individuals with a PhD or equivalent degree in bioengineering, biomedical engineering, or closely related disciplines for an open-rank, tenured/tenure-stream faculty position. We wish to recruit an individual with strong research accomplishments in Translational Bioengineering (i.e., leveraging basic science and engineering knowledge to develop innovative, translatable solutions impacting clinical practice and healthcare), with preference given to research focus on neuro-technologies, imaging, cardiovascular devices, and biomimetic and biorobotic design. It is expected that this individual will complement our current strengths in biomechanics, bioimaging, molecular, cellular, and systems engineering, medical product engineering, neural engineering, and tissue engineering and regenerative medicine. In addition, candidates must be committed to contributing to high quality education of a diverse student body at both the undergraduate and graduate levels.

[CLICK HERE FOR FURTHER DETAILS](#)

To ensure full consideration, applications must be received by June 30, 2019. However, applications will be reviewed as they are received. Early submission is highly encouraged.



NOTE

Detection of nanotesla AC magnetic fields using steady-state SIRS and ultra-low field MRI

RECEIVED
27 November 2019REVISED
16 March 2020ACCEPTED FOR PUBLICATION
8 April 2020PUBLISHED
28 May 2020Bragi Sveinsson^{1,2,4} , Neha Koonjoo^{1,2}, Bo Zhu^{1,2,3}, Thomas Witzel^{1,2} and Matthew S Rosen^{1,2,3}¹ A. A. Martinos Center for Biomedical Imaging, Massachusetts General Hospital, Boston, MA, United States of America² Department of Radiology, Harvard Medical School, Boston, MA, United States of America³ Department of Physics, Harvard University, Cambridge, MA, United States of America⁴ Author to whom any correspondence should be addressed.E-mail: bsveinsson@mgh.harvard.edu

Keywords: MRI, MEG, functional, neuron, ultra-low field

Abstract

Objective. Functional magnetic resonance imaging (fMRI) is commonly used to measure brain activity through the blood oxygen level dependent (BOLD) signal mechanism, but this only provides an indirect proxy signal to neuronal activity. Magnetoencephalography (MEG) provides a more direct measurement of the magnetic fields created by neuronal currents in the brain, but requires very specialized hardware and only measures these fields at the scalp. Recently, progress has been made to directly detect neuronal fields with MRI using the stimulus-induced rotary saturation (SIRS) effect, but interference from the BOLD response complicates such measurements. Here, we describe an approach to detect nanotesla-level, low-frequency alternating magnetic fields with an ultra-low field (ULF) MRI scanner, unaffected by the BOLD signal.

Approach. A steady-state implementation of the stimulus-induced rotary saturation (SIRS) method is developed. The method is designed to generate a strong signal at ultra-low magnetic field as well as allowing for efficient signal averaging, giving a high contrast-to-noise ratio (CNR). The method is tested in computer simulations and in phantom scans. *Main results.* The simulations and phantom scans demonstrated the ability of the method to measure magnetic fields at different frequencies at ULF with a stronger contrast than non-steady-state approaches. Furthermore, the rapid imaging functionality of the method reduced noise efficiently. The results demonstrated sufficient CNR down to 7 nT, but the sensitivity will depend on the imaging parameters.

Significance. A steady-state SIRS method is able to detect low-frequency alternating magnetic fields at ultra-low main magnetic field strengths with a large signal response and contrast-to-noise, presenting an important step in sensing biological fields with ULF MRI.

1. Introduction

Non-invasive functional neuroimaging methods fall into two classes: hemodynamically based approaches, including blood oxygenation level dependent (BOLD), arterial spin labeling (ASL), cerebral blood volume (CBV) and dynamic susceptibility contrast (DSC) methods, and electrophysiologically-based approaches, including electro- and magnetoencephalography (EEG and MEG respectively) source imaging. Such methods have seen more widespread use than more invasive techniques, such as radionuclide imaging of blood flow and chemical dynamics. The most widely used MRI-based functional magnetic resonance imaging (fMRI) technique uses the BOLD

relaxation effect as a proxy for neuronal activation as a means to obtain functional contrast in the brain [1–3]. Despite its profound impact as a tool for the advancement of neuroscience via the understanding of human brain activity, the latency of the hemodynamic response makes localization of signal sources above 1 Hz challenging using the signal from conventional BOLD fMRI [4]. In contrast, MEG provides functional brain imaging with high temporal resolution by direct measurement of magnetic fields produced by postsynaptic currents [5]. While having superior temporal resolution to fMRI, MEG measures these tiny biological magnetic fields at the scalp, typically with arrays of superconducting quantum interference device (SQUID) magnetometers. Obtaining

volumetric information of activated regions inside the brain requires complex numerical estimation of the field sources, limiting the spatial accuracy of the technique [6, 7].

Techniques that combine the direct magnetic detection of MEG with the spatial resolution of MRI have been developed, and are broadly referred to as neuronal current (NC) MRI. In these approaches, the magnetic fields induced by neuronal currents in the brain directly produce MRI contrast in an appropriately sensitive imaging sequence [8, 9]. While the currents from single neurons appear to be too weak to be detected, neuronal bundles have been estimated to produce fields of approximately 0.1–1 nT within a 1 mm³ voxel, possibly strong enough for ensemble detection [10]. Various approaches to NC MRI have been explored [9, 11–19]. These have often involved imaging contrast from spin dephasing effects that result from the minuscule change in the net magnetic field during a burst of neuronal current.

A promising, alternative method for NC MRI is based on the stimulus-induced rotary saturation (SIRS) effect [20]. With this technique, proton magnetization is aligned in the transverse plane with a spin-lock (SL) pulse of amplitude B_{SL} , effectively putting the magnetization in a doubly-rotating reference frame with Larmor frequency γB_{SL} [21]. The presence of a neuronal ‘stimulus’ magnetic field of frequency $f_{stim} = \gamma B_{SL}/2\pi$ will tip the magnetization away from the SL pulse. A preparation module, applying an SL pulse of length T_{SL} , will then result in a magnetization tipped by the angle $\alpha_{SL} = \gamma B_{stim} T_{SL}$, where B_{stim} is the strength of the stimulus field. The preparation module can then be followed by a fast imaging acquisition, such as single-shot echo-planar imaging (EPI), giving a contrast difference in regions that experienced a stimulus field of the right frequency during the preparation.

SIRS and similar spin-lock based sequences have given a clear improvement on prior methods for NC MRI and hold great promise, giving good results in phantom experiments [22–26]. Positive *in vivo* experiments using SIRS have often proven challenging [27, 28], possibly due to the presence of magnetic susceptibility BOLD contrast within the region with neuronal current, dominating the smaller SIRS contrast, which is inherently small due to the low amplitude of the neuronal field. Recently, positive *in vivo* results have been reported where the BOLD effect is accounted for in post-processing [29]. However, a method which is not confounded by BOLD contrast would still be useful as it would not require such post-processing steps. This could potentially be achieved by performing SIRS at a very low magnetic field, where the BOLD effect is negligible [30].

In this work, we investigate the performance of SIRS at an ultra-low field (ULF) of 6.5 mT [31]. We apply the SIRS technique in a novel steady-state

implementation which is designed for rapid imaging and results in an improved contrast-to-noise ratio (CNR). We demonstrate results from Bloch simulations and in phantoms, and describe possible *in vivo* experiments.

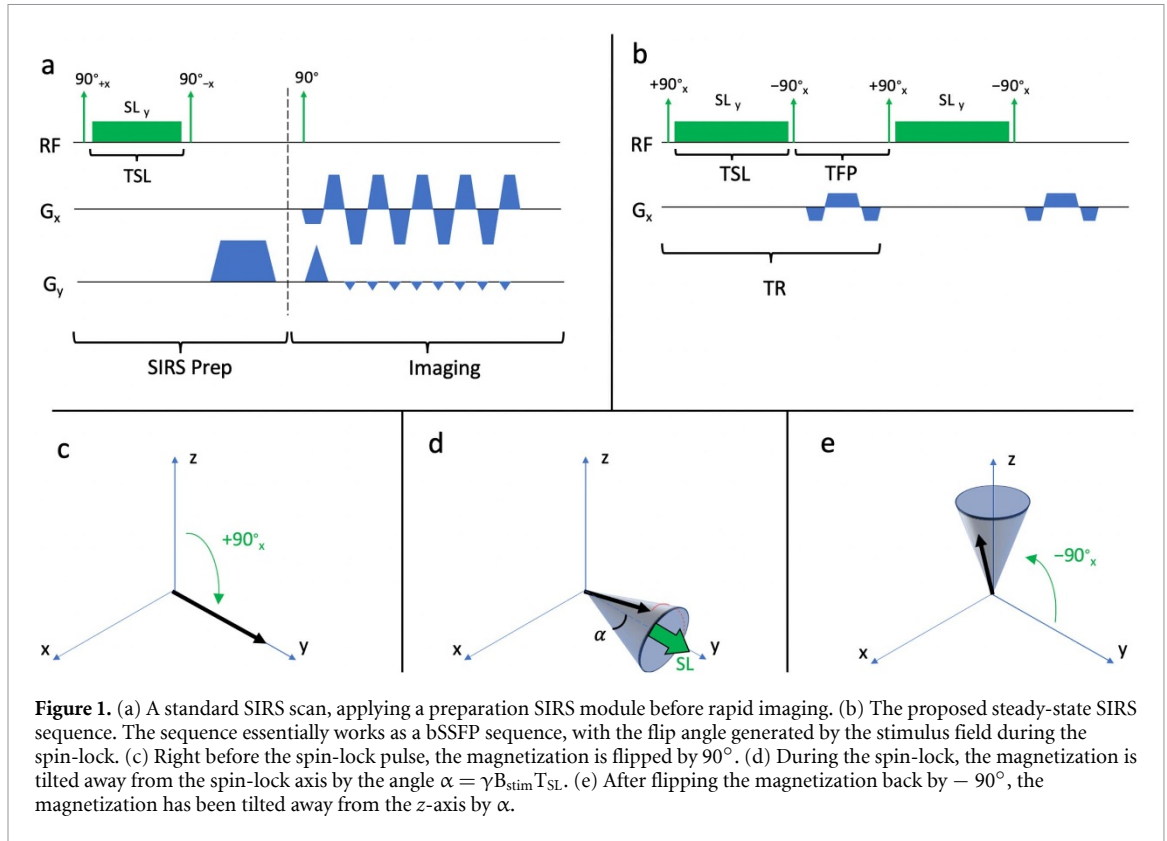
2. Methods

2.1. Sequence design

Schematics of the MRI sequence design and the resulting behavior of the magnetization are shown in figure 1. In the original SIRS implementation on a 3T scanner, a spin-lock (SL) preparation module, followed by a spoiler gradient, was implemented before a rapid 2D EPI scan, as shown in figure 1(a). To enable detection at ULF, our design goal was to maximize the contrast-to-noise ratio, $CNR = \delta/\sigma$, where δ is the difference in signal amplitude between acquisitions with and without stimulus, and σ is the standard deviation of the background noise. The design also needed to account for the ULF system having a maximum gradient amplitude of 1 mT m⁻¹ [31], making fast k-space traversal and time-efficient high SNR 2D imaging challenging.

As a ULF alternative to 2D EPI SIRS, we leveraged the efficiency of steady-state imaging at ULF [31] and developed a new steady-state sequence using SIRS as shown in figure 1(b). The sequence consists of a rapid application of a SIRS module every repetition time (TR), which consist of a 90°_x pulse, an SL pulse along the *y*-axis, and a 90°_{-x} pulse. If the spin is on resonance and no stimulus field is present, no tip will be experienced during the SL module, producing no transverse magnetization and therefore no signal will be generated. In the presence of a stimulus field of frequency $f_{stim} = \gamma B_{SL}/2\pi$ and magnitude B_{stim} , however, the SL module will effectively give a tip of angle $\alpha = \gamma B_{stim} T_{SL}$. The sequence will thus act as a balanced Steady-State Free Precession (bSSFP) sequence with flip angle α . It is important to note that during the spin-lock pulse, the magnetization will rotate about the spin-lock axis with frequency f_{SL} . To prevent phase accumulation during the spin-lock, the spin-lock should ideally be applied for a duration of $T_{SL} = n/f_{SL}$, where n is an integer.

This sequence can generate a large contrast δ even though α will typically be very small. It is well known from bSSFP theory that even a small tip angle can result in a large steady-state signal assuming little or no phase difference accumulates between the magnetization and the excitation pulses during each repetition time TR [32]. Furthermore, the rapid imaging and steady-state nature of the sequence allows for efficient signal averaging which is a requirement at ULF, resulting in a smaller σ and thus a larger CNR. Additionally, as bSSFP generally creates a larger signal when T_1/T_2 is small, the steady-state sequence has particularly good efficiency in a ULF scanner as T_1/T_2 can approach unity at very low fields [33].



2.2. Signal simulations

The steady-state SIRS sequence was simulated in MATLAB using Bloch simulations over a range of values for the stimulus field strength B_{stim} and frequency f_{stim} , with the sequence sensitized to an SL frequency of $f_{\text{SL}} = 40$ Hz with an SL duration of 25 ms. The simulation parameters are shown in table 1. The stimulus field was applied during the whole SL pulse. The Bloch equations used in the doubly rotating frame are as follows [20]:

$$\frac{dM}{dt} = \gamma M \times \left[B_{\text{total}} \left(1 - \frac{2\pi f_{\text{stim}}}{\gamma |B_{\text{total}}|} \right) + B_{\text{stim}} \right] - R(M - M_\rho),$$

where

$$R = \begin{pmatrix} \frac{1}{T_2^*} & 0 & 0 \\ 0 & \frac{1}{T_2^*} & 0 \\ 0 & 0 & \frac{1}{T_{1\rho}} \end{pmatrix}.$$

M_ρ is the equilibrium magnetization in the rotating frame, which can be assumed to be very small and in this work was assumed to be zero for simplicity. The B_{total} field includes both the main magnetic field B_0 as well as any field changes included to model off-resonance. Furthermore, in our analysis of the signal behavior at ULE, assumptions were made of $T_2^* = T_2$ and $T_{1\rho} = 2/(1/T_1 + 1/T_2)$ [34].

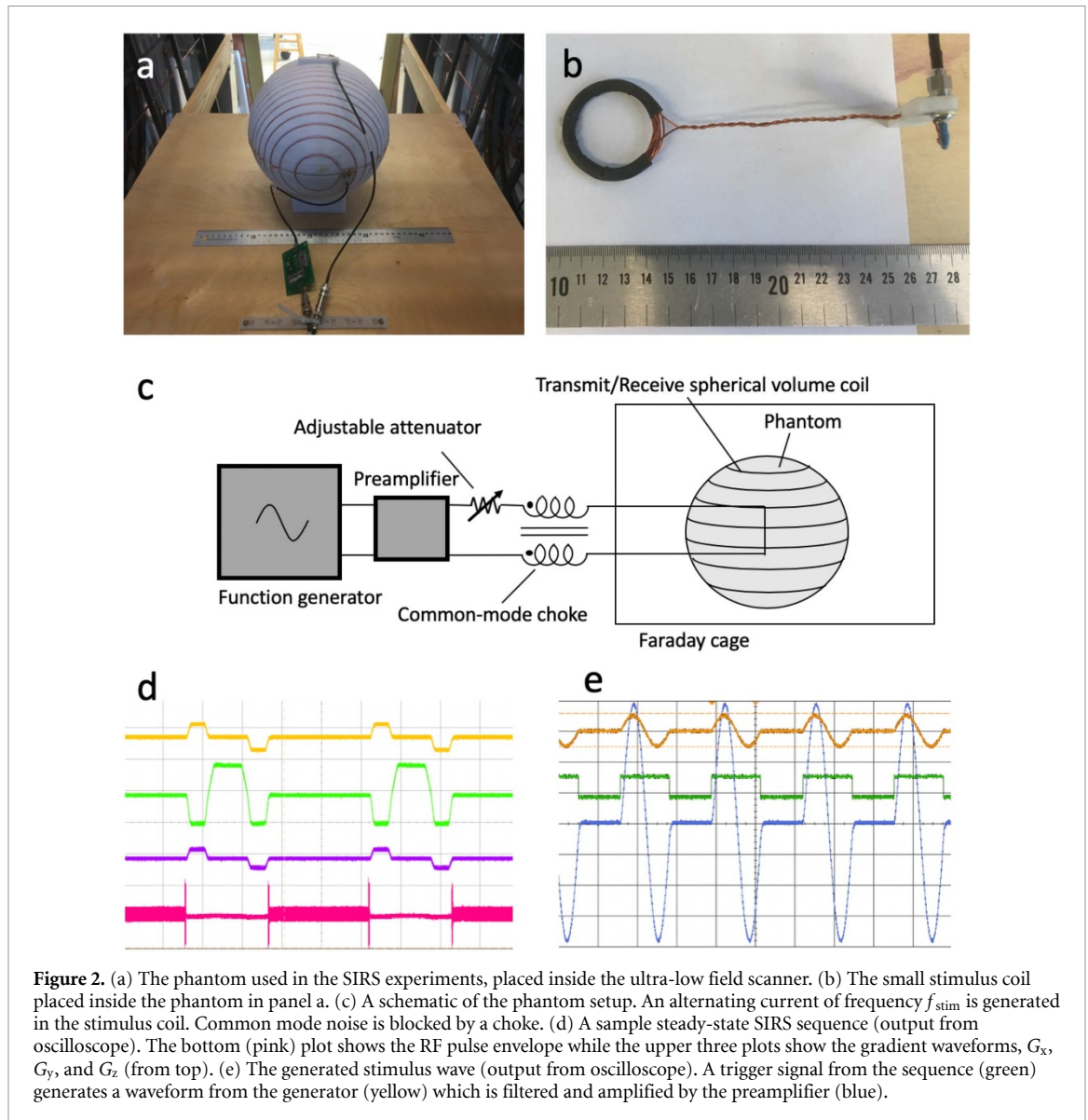
2.3. Experimental design

Experiments were performed on our 6.5 mT ULF scanner [31] using a phantom as shown in figure 2.

Table 1. Parameters for simulations and scans. f_{SL} : Spin-lock frequency; T_{SL} : Spin-lock duration; B_{stim} : Stimulus field magnitude; T_{FP} : Time between spin-lock modules; T_{RF} : RF pulse duration; f_{stim} : Stimulus field frequency; N_{av} : Number of averages. When altering B_{stim} , f_{stim} was kept fixed at f_{SL} . When altering f_{stim} , B_{stim} was kept fixed at 40 nT.

	Simulations	Phantom	
f_{SL} [Hz]	40	40	50
T_{SL} [ms]	25	25	20
B_{stim} [nT]	0:1:40	0:5:40	
T_{FP} [ms]	16.8	16.8	
T_{RF} [ms]	0.3	0.3	
f_{stim} [Hz]	0:2:120	25–120	
N_{av}	40	40	
FOV [cm ³]	—	28 × 28 × 20	
Matrix size	—	64 × 64 × 19	
k-space sampling fraction	—	0.5	
T_1 [ms]	630	630	
T_2 [ms]	625	625	
Scan time [mm:ss]	—	18:00	17:00

This 20 cm diameter spherical phantom was 3D printed (figure 2(a)) from polycarbonate (Stratasys Fortus 360 mc). An insulated, 20-gauge, 5 × 39 × 42 AWG FEP insulated litz wire (New England Wire Technologies, Lisbon, NH, USA) was wound in grooves on the surface of the phantom to form a single channel transmit-receive coil, which was capacitively tuned to a frequency of 276 kHz, corresponding to a 6.5 mT magnetic field, with a Q factor of 30 and matched to 50 Ohms. This modest Q at our low Larmor frequency allows for a readout bandwidth of about 10 kHz. The phantom was filled with CuSO₄-H₂O solution at a



concentration that resulted in a measured T_1 and T_2 of 630 ms and 625 ms in a 6.5 mT field, respectively. A smaller ‘stimulus coil’ (figure 2(b)), made of 19-gauge insulated magnet wire (MWS Wire Industries), was inserted into the phantom to serve as a proxy neuronal current (NC). This stimulus coil is a 10-turn circular loop with a 4 cm diameter, oriented such that the field produced by the stimulus coil is parallel to the scanner B_0 axis. The location of the stimulus coil within the phantom was determined with a reference bSSFP scan. The stimulus coil was connected to a frequency synthesizer (Stanford Research Systems DS345) through a low-noise voltage preamplifier (Ithaco 1201) and a variable attenuator. Using this setup, a sinusoidal current could be passed through the stimulus coil and the amplitude and frequency could be varied. The phantom was placed in the ULF scanner, which was located inside a Faraday cage. A common-mode choke on the coaxial transmission line to the stimulus coil before it entered the scan room eliminated any unwanted environmental

noise. The relationship between the voltage amplitude generated by the wave generator and the magnetic field produced by the coil was calibrated by doing a series of measurements with a 3-axis flux gate magnetometer (Bartington Mag-03MCT1000). The results matched numerical calculations from the Biot-Savart law very closely. As in the simulations, the phantom scans were run with multiple values of B_{stim} and f_{stim} , as shown in table 1. To further evaluate the measured signal at off-resonance frequencies, additional measurements were performed using a lower resolution of a $32 \times 32 \times 19$ imaging matrix over a $28 \text{ cm} \times 28 \text{ cm} \times 20 \text{ cm}$ FOV and $TR = 54 \text{ ms}$, $TSL = 41 \text{ ms}$, $TFP = 13.3 \text{ ms}$, $f_{SL} = 100 \text{ Hz}$, $N_{av} = 120$, $f_{stim} = 80\text{--}120 \text{ Hz}$ and $B_{stim} = 15 \text{ nT}$ and 75 nT at $\Delta f = -25 \text{ Hz}$ off-resonance and compared to simulations.

2.4. Neuronal field generation and sequence timing

The steady-state SIRS pulse sequence provided a trigger signal to the synthesizer at the start of each

spin-lock pulse to output a sinusoidal wave with an integer number of wavelengths at frequency f_{stim} . This number was set to the minimum such that the wave lasted throughout the spin-lock pulse. In the steady-state SIRS sequence, maximum signal is achieved when no phase difference accumulates between the magnetization and the stimulus wave over multiple TRs. This is similar to a normal bSSFP sequence, which gives signal ‘spikes’ at low flip angles and no phase accrual. In the phantom experiments, this was achieved by timing the spin lock pulse such that $T_{\text{SL}} = n/f_{\text{SL}}$, where n is an integer. The magnetization then accumulates a phase of $\phi_{\text{M}} = 2\pi f_{\text{SL}} T_{\text{SL}} = n2\pi$ during the spin-lock by precessing around the SL axis, and ideally no phase outside the spin-lock assuming it is on-resonance, and will therefore be in phase with the next RF pulse generated by the console (Tecmag Redstone).

2.5. Image analysis

A difference image was created by subtracting the SIRS image acquired with no stimulus from the SIRS image acquired with a stimulus current on. The contrast δ was defined as the average amplitude difference of a 3×3 -pixel ROI in the center of the stimulus coil, while the noise standard deviation σ was calculated from a similar ROI away from the stimulus coil and computing the standard deviation of its pixels. This enabled calculation of the $\text{CNR} = \delta/\sigma$.

2.6. Simulated comparison to other SIRS contrast mechanisms

Computer simulations were performed to compare the generated signal from the proposed steady-state method to that generated by a non-steady-state approach under the same imaging conditions and a long stimulus wave. Such approaches would generate one large tip during the stimulus, and utilize either the component orthogonal or parallel to the spin-lock pulse for imaging. As described, during the spin-lock pulse, the magnetization gets tilted away from the spin-lock axis by the angle $\alpha = \gamma B_{\text{stim}} T_{\text{SL}}$. At the same time, the magnetization component along this axis, M_{\parallel} is decaying with time constant $T_{1\rho}$ while the magnetization perpendicular to the spin-lock axis M_{\perp} is decaying with time constant $T_2^* > T_2 > T_{1\rho}$. In a ULF scanner, we can make the approximation that both components are decaying with $T_{1\rho}$, which then serves as a conservative estimate of the decay time. The magnetization during the spin-lock will then decay by the factor $e^{-T_{\text{SL}}/T_{1\rho}}$. In the original implementation of the SIRS technique [20], the signal contrast is the parallel difference $\Delta M_{\parallel} = e^{-T_{\text{SL}}/T_{1\rho}} (1 - \cos(\gamma B_{\text{stim}} T_{\text{SL}})) M_0$. This can easily be shown to be maximized when $T_{\text{SL}} \approx 2T_{1\rho}$ with a maximum of $\Delta M_{\parallel, \text{max}} \approx 2(e^{-1} \gamma B_{\text{stim}} T_{1\rho})^2 M_0$. Another approach is to use the M_{\perp} component, resulting in a contrast of $\Delta M_{\perp} =$

$e^{-T_{\text{SL}}/T_{1\rho}} \sin(\gamma B_{\text{stim}} T_{\text{SL}}) M_0$ which has a maximum of $\Delta M_{\perp, \text{max}} \approx e^{-1} \gamma B_{\text{stim}} T_{1\rho} M_0$ when $T_{\text{SL}} \approx T_{1\rho}$. These maxima can be viewed as the upper theoretical limits of the two signal components, in the case of a uniform decay of $T_{1\rho}$ and a long stimulus wave. These upper signal limits were compared to the signal generated by the steady-state sequence, computed with Bloch simulations.

3. Results

Simulation results of the signal behavior in the steady-state SIRS sequence are shown in figure 3 for a range of B_{stim} , f_{stim} , and off-resonance values Δf as shown in table 1. The results indicate a frequency response with a main lobe centered on f_{SL} and giving a zero value at $2/T_{\text{SL}}$, followed by smaller sidelobes. Without a stimulus field, figure 3(b) shows a band of low signal intensity for reasonably small values of the off-resonance Δf . With significant off-resonance, the magnetization will not only precess around the spin-lock axis, but around the vector sum $\mathbf{B}_{\text{total}} = 2\pi/\gamma (f_{\text{SL}} + \Delta f)$ during the spin-lock pulse, and around $2\pi/\gamma \Delta f$ outside the spin-lock. This results in a non-zero tip during each TR, giving a steady-state signal response in the upper and lower regions of figures 3(a)–(b).

Sample images acquired in the phantom are shown in figure 4. The images show a dark band with very low signal across the phantom, similar to the low-intensity band in figures 3(a)–(b). In this region, the spins are very nearly on-resonance with the transmit frequency, which together with the spin-lock frequency being $f_{\text{SL}} = 1/T_{\text{SL}}$ results in no net phase accrual during the TR and thus no NMR signal. With perfect field homogeneity, the whole phantom would be dark, while in our experiment the dark band can be thought of as an effective field of view with the desired signal behavior. With the stimulus field present, the magnetization is tipped away from the spin-lock axis by $\alpha = \gamma B_{\text{stim}} T_{\text{SL}}$ every TR, resulting in a net steady-state signal.

The phantom results for various B_{stim} and f_{stim} values, described in table 1, are shown in figure 5. The measurements with varying f_{stim} (figures 5(a), (c)) demonstrate a signal peak when $f_{\text{stim}} = f_{\text{SL}}$. The signal response curves are narrower than their corresponding simulations, with a full width at half maximum (FWHM) of about 20–30 Hz. Additionally, the measured signal response curves do not show any clear indication of sidelobes. The B_{stim} measurements (figures 5(b), (d)) demonstrate an approximately linear response as a function of stimulus field magnitude. For both stimulus frequencies, the slope of the trend line of CNR as a function of stimulus field is about 0.14 nT^{-1} .

Figure 6 shows a comparison of the signal magnitude generated by our steady-state method to non-steady-state approaches in the presence of

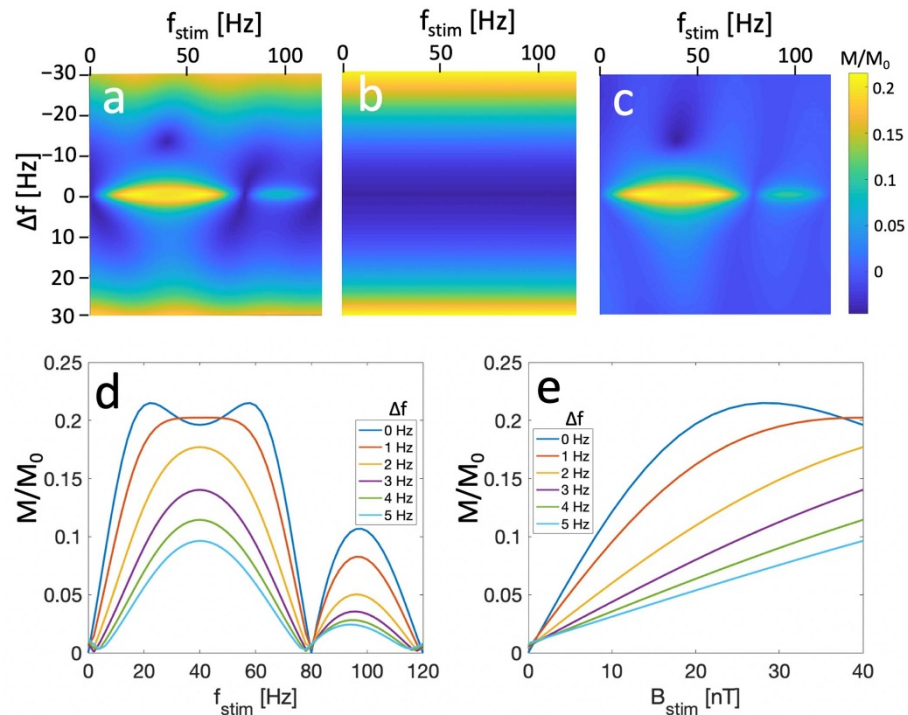


Figure 3. (a) The steady-state SIRS response with $f_{SL} = 40$ Hz, $B_{stim} = 40$ nT, over a range of f_{stim} and off-resonance frequencies Δf . (b) The same simulations with no stimulus field. (c) The difference between panels a and b. (d) Cross sections of the surface in panel a. The different colors represent off-resonance frequencies Δf . (e) The signal response of a steady-state SIRS sequence with $f_{SL} = 40$ Hz and $f_{stim} = 40$ Hz over a range of stimulus field strengths B_{stim} for several off-resonance frequencies Δf .

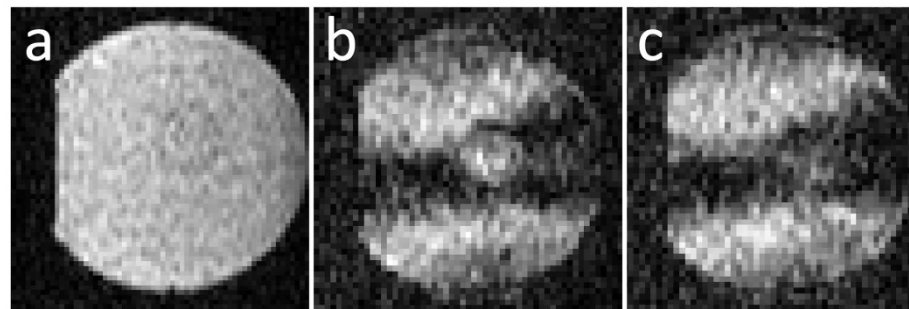


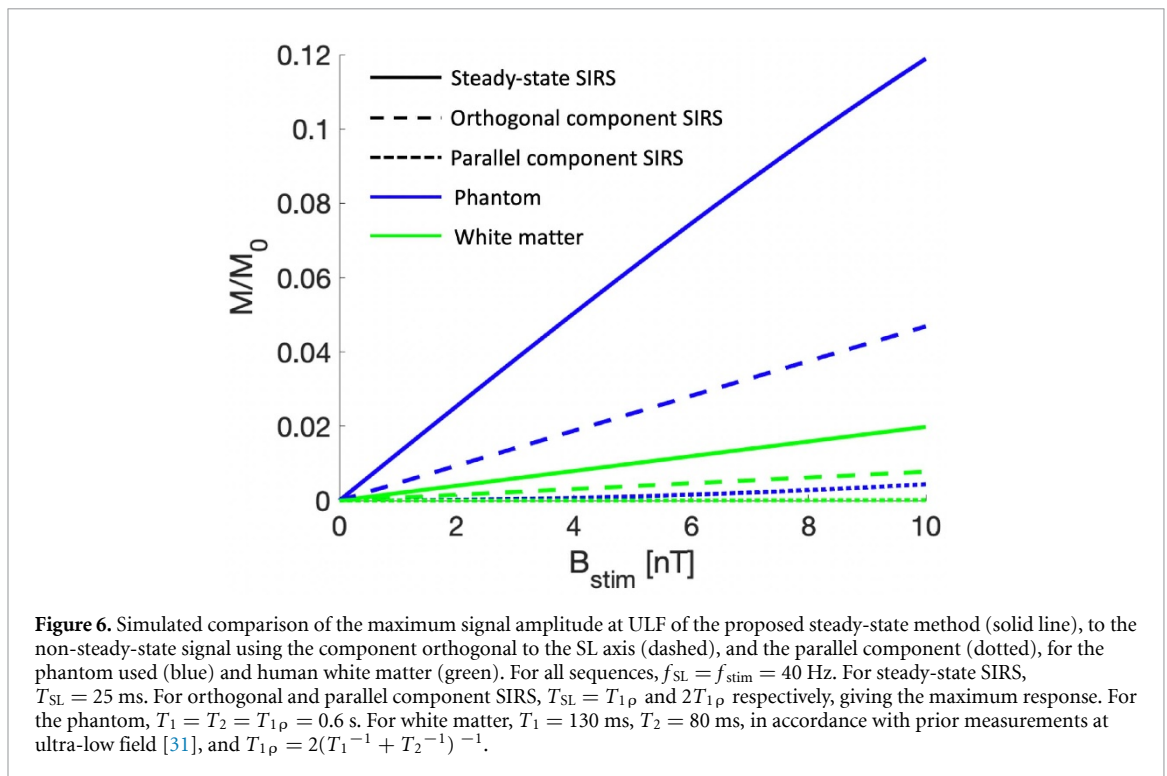
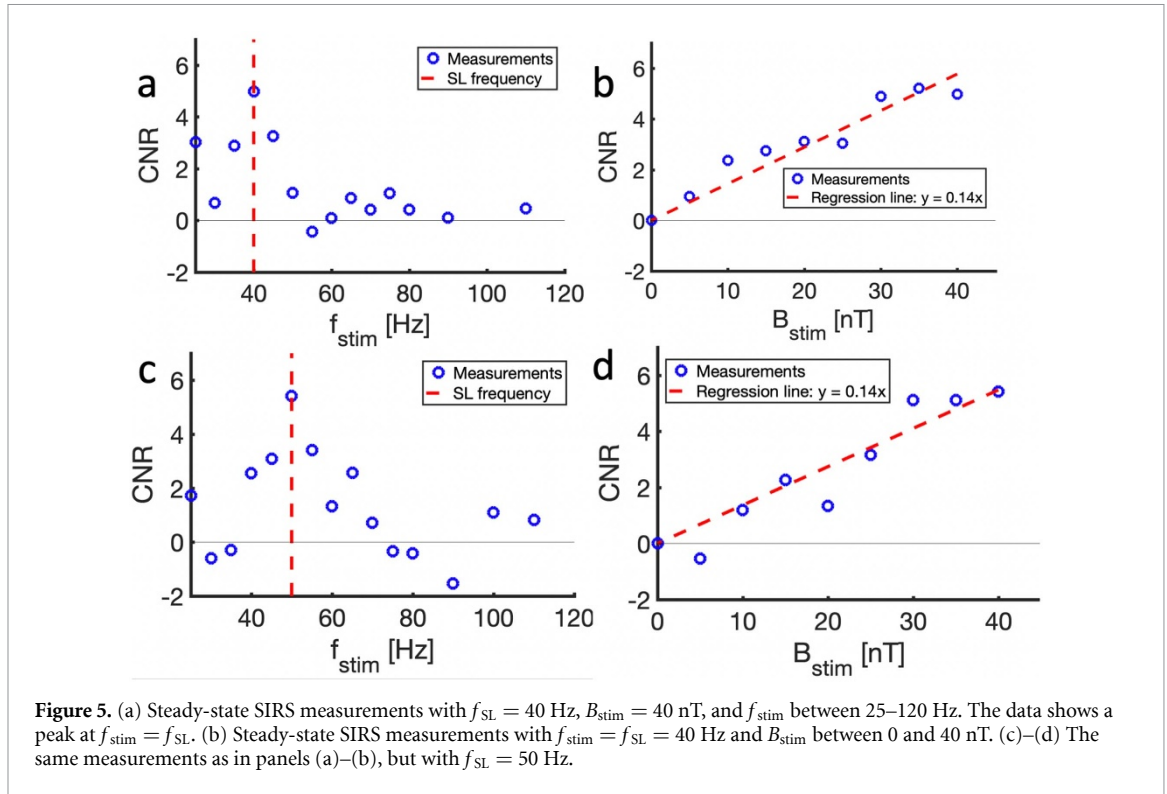
Figure 4. Typical results from phantom scans at 40 Hz. (a) A reference bSSFP image of the water-filled phantom (voxel size: $3.6 \text{ mm} \times 3.6 \text{ mm} \times 9.5 \text{ mm}$). The outline of the stimulus coil can be seen. (b) A steady-state SIRS image with a stimulus with $B_{stim} = 40$ nT and $f_{stim} = f_{SL} = 40$ Hz. Note that as the spins get further off-resonance, we see a sharp transition from a signal void to a high signal, similar to figures 3(a)–(b) (a dark band). With perfect field homogeneity, the whole phantom would be dark. (c) The same acquisition as in panel b, but with no stimulus current applied.

a long stimulus wave. Steady-state SIRS clearly gives a stronger signal than the other methods, mainly due to the signal decay taking place during the RF pulse from both $T_{1\rho}$ and T_2 relaxation. Furthermore, the rapid signal averaging enabled by the method reduces noise, further improving the CNR.

The results from the off-resonance measurements are shown in figure 7. The measurements and the simulations are in good agreement, and show a negative contrast slightly below the frequency f_{SL} . The results also demonstrate a ripple response when f_{stim} is more than approximately 10 Hz from f_{SL} .

4. Discussion

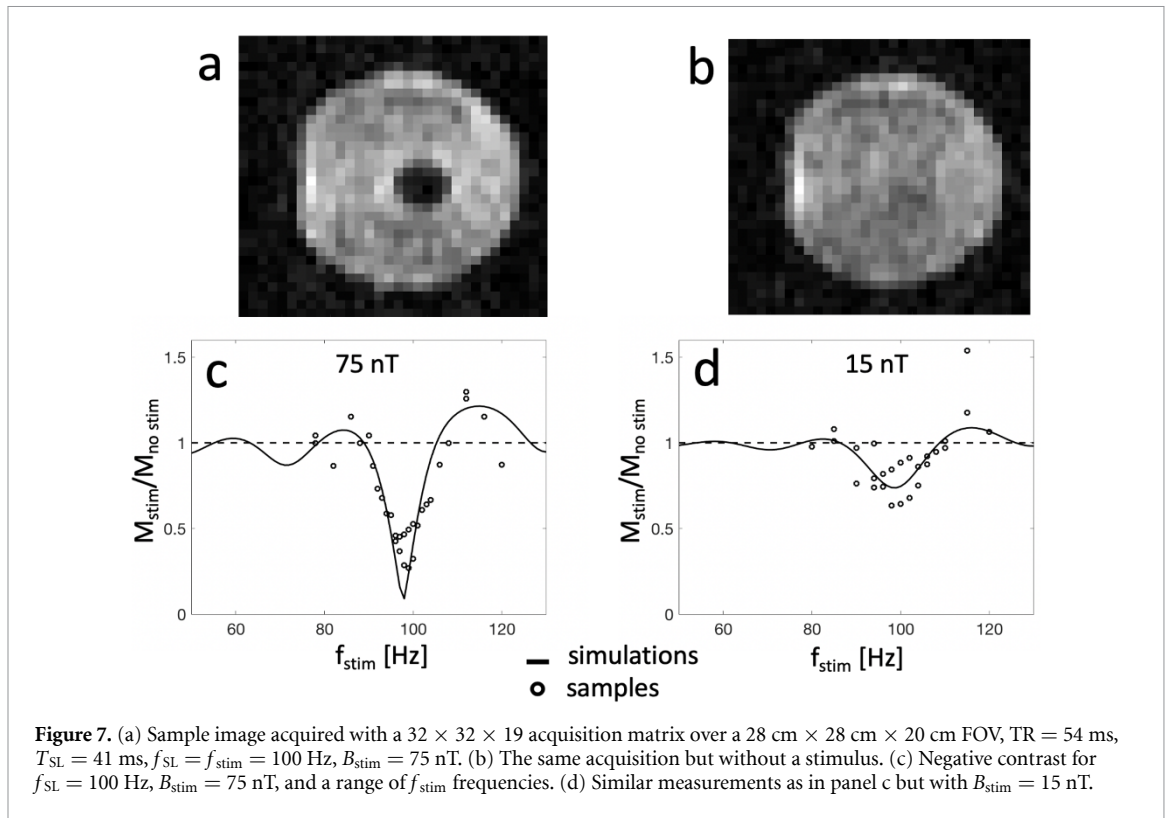
In this work, we have explored using the SIRS mechanism for detecting small oscillating magnetic fields in a ULF scanner. The method is based on a novel steady-state implementation of SIRS, designed to provide an optimal response in a ULF scanner with low gradient strength. The method has been shown to give a strong contrast at the targeted stimulus frequencies, as well as being rapid enough to allow for efficient signal averaging to overcome low Boltzmann polarization at ULF and reduce noise. This results in a high contrast-to-noise ratio. The method was



tested in simulations and in phantom scans. While bSSFP has been combined with spin-lock techniques before [35], the presently described implementation is specifically designed for highly SNR-efficient current detection, combining the high SNR efficiency of bSSFP and the sensitivity of SIRS to sense small external magnetic fields.

Our method utilizes several advantages of the ULF system, one being its low specific absorption rate

(SAR). For example, in the scans with $f_{SL} = 40$ Hz, the spin lock pulse had a duration of 25 ms, applied every TR with an approximate duration of 42 ms. An on-resonance 40 Hz spin lock pulse of this duration and duty cycle can be shown to risk exceeding FDA SAR limits at a 3T (128 MHz) system [36], while for a ULF system at 276 kHz the SAR is negligible, as it scales with the square of the main field. This difference would become even more pronounced with



faster imaging gradients, giving shorter TR. Furthermore, the sequence requires the magnetization to be no more than about $\pm 5 \text{ Hz}$ off-resonance, as can be seen in figure 3(a). At 3T, this corresponds to a fractional B_0 homogeneity of about $\pm 0.04 \text{ ppm}$, a challenging engineering constraint for any magnet, let alone the inevitable effects of magnetic susceptibility gradients *in vivo*. At the 6.5 mT ULF system, however, this corresponds to a rather relaxed $\pm 18 \text{ ppm}$ fractional homogeneity requirement on the scanner magnetic field. Another benefit of the ULF system is that smaller interfering fields will be created by induced currents in vessels such as arterioles that pulsate in the magnetic field. While we estimate this effect to be small even under clinical field strengths and would only result in interference at the vascular pulsating frequency, it is of even less concern at ULF, where we estimate it to be approximately 6 orders of magnitude below desired sensitivity levels. Additionally, the open design of the ULF system allows the patient to be scanned under different angles relative to the B_0 field. This can be beneficial, as the SIRS method is only sensitive to fields parallel to the main field.

While the phantom results agree with the simulation results in important ways, some discrepancies are also apparent by comparing figures 3 and 5. The f_{stim} response lobe is narrower in the phantom and does not exhibit clear sidelobes, and the B_{stim} response appears increasing and mostly linear, while the simulations show a response that tapers off at high values of B_{stim} . These effects could be the result of the large voxel size used in the scan, which could make

B_0 , B_1 , B_{SL} , and B_{stim} nonuniform within the voxel. In particular, the voxel is large in the slice dimension (roughly 1 cm), which means that large parts of the voxel are distant from the plane of the coil and experience lower B_{stim} . Furthermore, even though an effort was made to make the coil plane perpendicular to B_0 , there will inevitably be some misalignment between the two. This results in a lower effective field, as only the B_{stim} component parallel to B_0 contributes to the SIRS effect.

As described, in the phantom scans the pulse sequence triggers the synthesizer that drives B_{stim} , and the synthesizer generated a number of wavelengths at the desired frequency, as shown in figure 2. Alternatively, the sequence could measure a continuous wave. In this case, the sequence should ideally be timed such that the phase $\phi_{\text{stim}} = 2\pi f_{\text{stim}} \text{TR}$ accumulated by the stimulus wave over the TR satisfies $\phi_{\text{stim}} = \phi_{\text{M}} + n2\pi$, where ϕ_{M} is the phase accumulated by the magnetization. This is achieved if $f_{\text{stim}} = f_{\text{SL}}$, $T_{\text{SL}} = n/f_{\text{SL}}$, and the time in between SL modules is $TFP = m/f_{\text{stim}}$, where n and m are integers, and no additional phase is acquired by the magnetization due to off-resonance effects.

The simulations and measurements appeared to agree equally well on-and off-resonance. Figures 3(a) and 7 demonstrate that our sequence can produce a negative contrast in the presence of a stimulus field when run with a slight shift Δf away from resonance. Although this contrast can be quite strong, it is not as useful as the positive contrast mechanism as it gives maximum contrast slightly away from the spin-lock

frequency f_{SL} while also having a large ripple response away from the maximum contrast. Furthermore, the agreement between measurements and simulations did not depend on the stimulus coil size. This is demonstrated in supplementary figure S1, showing the response from a smaller stimulus coil with an 8 mm diameter, giving a very similar response as the larger 40 mm coil described in the Methods section. This larger coil was preferred for the experiments due to the ease of measuring its center field and thus calibrating the coil.

The measurement technique described in this work is sensitive primarily to the magnetic field generated by the primary currents in the dendrites of pyramidal cells of the cortex, that due to their parallel alignment and synchronous population in the tens if not hundreds of thousands of neurons provide dipolar magnetic fields of the strength detectable by our techniques. In that regard our technique is very similar to magnetoencephalography (MEG) [6]. MEG suffers a cancellation scenario due to volume currents when the dipole is radial in a conducting sphere. The technique proposed in this work is not affected by this, as we are detecting inside the conducting medium. There is another scenario, where volume currents could affect our measurements, when the sources are extremely close to conductivity boundaries. On the scale of any mammalian brain the number of locations affected by this would be negligible [17]. The proposed technique detects magnetic fields of the primary dipole, and the magnetic field of the volume return currents, especially at distal regions has no significant effect on our measurements.

The ultimate goal of magnetic field detection with methods such as SIRS is to measure biological magnetic fields in the brain. Results from the literature estimate that sensitivity to fields in the range of 0.1–1 nT is necessary with an MRI imaging scale of about 1 mm [10, 37–39]. For the ultra-low field scanner, the average magnetic field from a neuronal bundle within a voxel would likely be smaller due to the larger voxel size. A method to detect human brain activity would therefore very likely need to be sensitive to fields no larger than 0.1 nT. For a 3×3 -pixel ROI like the one used in this work, a $CNR = 1$ has been estimated as necessary for clear contrast, based on the Rose model [40, 41]. Figure 5 shows the steady-state SIRS method at ultra-low field giving $CNR = 1$ at about $B_{stim} = 7$ nT. Furthermore, as is demonstrated in the simulations in figure 6, the lower values of T_1 and T_2 in white matter would likely reduce the generated signal amplitude by approximately a factor of 5. This indicates that our method is likely to be insufficiently sensitive for *in vivo* imaging in the described ULF setting. Running the method at a higher field, yielding better SNR, or with increased gradient strength, allowing shorter TR, could make the method sufficiently sensitive to measure biological-strength fields.

The field could likely be increased by an order of magnitude while retaining insensitivity to BOLD effects and without reaching SAR limits. The CNR can also be improved with more signal averaging but this can increase scan time to unacceptable durations. With enough sensitivity, the method could potentially be tested by playing an auditory stimulus to a subject in the form of a ‘click train’. Such a stimulus has been shown to result in an auditory steady-state response, being particularly sensitive to frequencies around 40 Hz [42–44]. This would likely be the most feasible way of testing the method on human subjects, but care would need to be taken to use pneumatic headphones that do not produce interfering electromagnetic fields close to the subject.

Our method has certain limitations. As already described, the sequence requires phase coherence in the stimulus wave at the start of each spin-lock period. This can either be achieved with coherent wave bursts or with a long, synchronous wave. Additionally, the sequence is inherently sensitive to errors in B_0 and B_1 , which require careful measurements and calibration of these parameters. As described, the magnetic field homogeneity required for the method is difficult to achieve in a clinical high-field scanner but feasible at the ultra-low field scanner used. However, this scanner was sensitive to external field interference, such as from large metal objects in the external environment of the scanner shimming the magnet. An effort was made to keep any effects from such external shimming (e.g. cars parked nearby) to a minimum.

5. Conclusion

We have developed a steady-state implementation of the SIRS mechanism, designed to give strong CNR at ultra-low fields with limited gradient strengths. Simulations and phantom scans demonstrated a strong signal response. With operation at larger magnetic field (but still in the low-field regime) or incorporation of higher gradient amplitudes, the method could potentially provide sensitivity to biological fields.

Acknowledgments

DARPA 2016D006054

ORCID iD

Bragi Sveinsson  <https://orcid.org/0000-0001-8109-0404>

References

- [1] Ogawa S, Lee T M, Kay A R and Tank D W 1990 Brain magnetic resonance imaging with contrast dependent on blood oxygenation *Proc. Natl. Acad. Sci.* **87** 9868–72
- [2] Ogawa S, Tank D W, Menon R *et al* 1992 Intrinsic signal changes accompanying sensory stimulation: functional brain

- mapping with magnetic resonance imaging *Proc. Natl. Acad. Sci.* **89** 5951–5
- [3] Kwong K K, Belliveau J W, Chesler D A *et al* 1992 Dynamic magnetic resonance imaging of human brain activity during primary sensory stimulation *Proc. Natl. Acad. Sci.* **89** 5675–9
 - [4] Lewis L D, Setsompop K, Rosen B R and Polimeni J R 2016 Fast fMRI can detect oscillatory neural activity in humans *Proc. Natl. Acad. Sci.* **113** E6679–85
 - [5] Cohen D 1972 Magnetoencephalography: detection of the brain's electrical activity with a superconducting magnetometer *Science* **175** 664–6
 - [6] Hämäläinen M, Hari R, Ilmoniemi R J, Knuutila J and Lounasmaa O V 1993 Magnetoencephalography—theory, instrumentation, and applications to noninvasive studies of the working human brain *Rev. Mod. Phys.* **65** 413–97
 - [7] Hämäläinen M and Ilmoniemi R J 1994 Interpreting magnetic fields of the brain: minimum norm estimates *Med. Biol. Eng. Comput.* **32** 35–42
 - [8] Hagberg G E, Bianciardi M and Maraviglia B 2006 Challenges for detection of neuronal currents by MRI *Magn. Reson. Imaging* **24** 483–93
 - [9] Bandettini P A, Petridou N and Bodurka J 2005 Direct detection of neuronal activity with MRI: fantasy, possibility, or reality? *Appl. Magn. Reson.* **29** 65–88
 - [10] Bodurka J and Bandettini P A 2002 Toward direct mapping of neuronal activity: MRI detection of ultraweak, transient magnetic field changes *Magn Reson Med.* **47** 1052–8
 - [11] Konn D, Gowland P and Bowtell R 2003 MRI detection of weak magnetic fields due to an extended current dipole in a conducting sphere: a model for direct detection of neuronal currents in the brain *Magn. Reson. Med.* **50** 40–9
 - [12] Chu R, de Zwart J A, van Gelderen P *et al* 2004 Hunting for neuronal currents: absence of rapid MRI signal changes during visual-evoked response *NeuroImage* **23** 1059–67
 - [13] Höfner N, Albrecht H H, Cassará A M *et al* 2011 Are brain currents detectable by means of low-field NMR? A phantom study *Magn. Reson. Imaging* **29** 1365–73
 - [14] Kim K, Lee S J, Kang C S, Hwang S M, Lee Y H and Yu K K 2014 Toward a brain functional connectivity mapping modality by simultaneous imaging of coherent brainwaves *NeuroImage* **91** 63–9
 - [15] Körber R, Nieminen J O, Höfner N *et al* 2013 An advanced phantom study assessing the feasibility of neuronal current imaging by ultra-low-field NMR *J. Magn. Reson.* **237** 182–90
 - [16] Luo Q and Gao J H 2010 Modeling magnitude and phase neuronal current MRI signal dependence on echo time *Magn. Reson. Med.* **64** 1832–7
 - [17] Sundaram P, Nummenmaa A, Wells W *et al* 2016 Direct neural current imaging in an intact cerebellum with magnetic resonance imaging *NeuroImage* **132** 477–90
 - [18] Truong T K, Wilbur J L and Song A W 2006 Synchronized detection of minute electrical currents with MRI using Lorentz effect imaging *J. Magn. Reson.* **179** 85–91
 - [19] Truong T K, Avram A and Song A W 2008 Lorentz effect imaging of ionic currents in solution *J. Magn. Reson.* **191** 93–99
 - [20] Witzel T, Lin F H, Rosen B R and Wald L L 2008 Stimulus-induced rotary saturation (SIRS): a potential method for the detection of neuronal currents with MRI *NeuroImage* **42** 1357–65
 - [21] Redfield A G 1955 Nuclear magnetic resonance saturation and rotary saturation in solids *Phys. Rev.* **98** 1787–809
 - [22] Halpern-Manners N W, Bajaj V S, Teisseyre T Z and Pines A 2010 Magnetic resonance imaging of oscillating electrical currents *Proc. Natl. Acad. Sci.* **107** 8519–24
 - [23] Chai Y, Bi G, Wang L *et al* 2016 Direct detection of optogenetically evoked oscillatory neuronal electrical activity in rats using SLOE sequence *NeuroImage* **125** 533–43
 - [24] Jiang X, Sheng J, Li H *et al* 2016 Detection of subnanotesla oscillatory magnetic fields using MRI *Magn. Reson. Med.* **75** 519–26
 - [25] Truong T K and Song A W 2006 Finding neuroelectric activity under magnetic-field oscillations (NAMO) with magnetic resonance imaging in vivo *Proc. Natl. Acad. Sci.* **103** 12598–601
 - [26] Nagahara S, Ueno M and Kobayashi T 2013 Spin-lock imaging for direct detection of oscillating magnetic fields with MRI: simulations and phantom studies *Adv. Biomed. Eng.* **2** 63–71
 - [27] Luo Q, Jiang X and Gao J H 2011 Detection of neuronal current MRI in human without BOLD contamination *Magn. Reson. Med.* **66** 492–7
 - [28] Sheng J, Liu Y, Chai Y, Tang W, Wu B and Gao J H 2016 A comprehensive study of sensitivity in measuring oscillatory magnetic fields using rotary saturation pulse sequences *Magn. Reson. Imaging* **34** 326–33
 - [29] Truong T K, Roberts K C, Woldorff M G and Song A W 2019 Toward direct MRI of neuro-electro-magnetic oscillations in the human brain *Magn. Reson. Med.* **81** 3462–75
 - [30] Nieminen J O, Zevenhoven K C J, Vesanen P T, Hsu Y C and Ilmoniemi R J 2014 Current-density imaging using ultra-low-field MRI with adiabatic pulses *Magn. Reson. Imaging* **32** 54–9
 - [31] Sarracanie M, Lapierre C D, Salameh N, Waddington D E J, Witzel T and Rosen M S 2015 Low-cost high-performance MRI *Sci. Rep.* **5** 1–9
 - [32] Carr H Y 1958 Steady-state free precession in nuclear magnetic resonance *Phys. Rev.* **112** 1693–701
 - [33] Bottomley P A, Foster T H, Argersinger R E and Pfeifer L M 1984 A review of normal tissue hydrogen NMR relaxation times and relaxation mechanisms from 1–100 MHz: dependence on tissue type, NMR frequency, temperature, species, excision, and age *Med. Phys.* **11** 425–48
 - [34] Abragam A 1961 *The Principles of Nuclear Magnetism* (Oxford: Oxford University Press)
 - [35] Witschey W R T, Borthakur A, Elliott M A *et al* 2009 Spin-locked balanced steady-state free-precession (sSSEFP) *Magn. Reson. Med.* **62** 993–1001
 - [36] Collins C M and Smith M B 2001 Calculations of B1 distribution, SNR, and SAR for a surface coil adjacent to an anatomically-accurate human body model *Magn. Reson. Med.* **45** 692–9
 - [37] Romani G L 1989 Fundamentals on neuromagnetism *Advances in Biomagnetism*, ed S J Williamson, M Hoke, G Stroink and M Kotani (Boston: Springer) pp 33–46
 - [38] Wikswo J P 1989 Biomagnetic sources and their models *Advances in Biomagnetism*, ed S J Williamson, M Hoke, G Stroink and M Kotani (Boston: Springer) pp 1–18
 - [39] Cassará A M, Maraviglia B, Hartwig S, Trahms L and Burghoff M 2009 Neuronal current detection with low-field magnetic resonance: simulations and methods *Magn. Reson. Imaging* **27** 1131–9
 - [40] Hendrick R E 2008 Signal, noise, signal-to-noise, and contrast-to-noise ratios *Breast MRI: Fundamentals and Technical Aspects* (New York: Springer)
 - [41] Rose A 1973 *Vision—Human and Electronic* (New York: Plenum Press)
 - [42] Gutschalk A, Mase R, Roth R *et al* 1999 Deconvolution of 40 Hz steady-state fields reveals two overlapping source activities of the human auditory cortex *Clin. Neurophysiol.* **110** 856–68
 - [43] Palmer A R and Russell I J 1986 Phase-locking in the cochlear nerve of the guinea-pig and its relation to the receptor potential of inner hair-cells *Hear Res.* **24** 1–15
 - [44] Palmer A R, Winter I M and Darwin C J 1986 The representation of steady-state vowel sounds in the temporal discharge patterns of the guinea pig cochlear nerve and primarylike cochlear nucleus neurons *J. Acoust. Soc. Am.* **79** 100–13